Experimental measurements and computational modeling of the flow field in an idealized human oropharynx

A.F. Heenan, E. Matida, A. Pollard, W.H. Finlay

Abstract The velocity field in the central sagittal plane of an idealized representation of the human oropharynx (HOP) during steady inspiration, simulating oral inhalation through an inhaler mouthpiece, was measured experimentally using endoscopic particle image velocimetry (PIV). Measurements were made at three flow rates: 15, 30, and 90 L/min, which correspond to a wide range of physiological conditions. Extensive tests were performed to verify the veracity of the PIV data. The flow was also modeled computationally using Reynolds-averaged Navier–Stokes (RANS) computational fluid dynamics (CFD) methods. The PIV data clearly indicate the complex nature of HOP flow, with three-dimensionality and several regions of separation and recirculation evident. Comparison of the experimental and computational results shows that, although the RANS CFD reproduces the basic features of the flow, it does not adequately capture the increased viscous effects at lower Reynolds numbers. The results demonstrate the need for more development and validation of CFD modeling, in particular RANS methods, in these flows.

1
Introduction

The flow field in the extra-thoracic airway is an important factor affecting particle (aerosol) deposition in the human respiratory system. The extra-thoracic airway acts as a filter, limiting the amount of an inhaled aerosol that enters the lungs. The proportion of aerosol deposited in the extra-thoracic airway varies dramatically, depending on a variety of parameters relating to both the flow field and the inhaled particles. Understanding and predicting extra-thoracic airway particle deposition is important in the study of the effects of environmental aerosols on human physiology, and also in the development of inhalation-based drug delivery systems.

The mechanics of extra-thoracic airway particle deposition can be separated into two parts: the flow field generated by the extra-thoracic airway geometry, and the interaction of the aerosol particles with this flow field. This separation can be seen in more sophisticated extra-thoracic airway deposition predictors, which first model (or simulate) the extra-thoracic airway flow field using computational fluid dynamics (CFD), then numerically "release" and track the paths of a large number of virtual particles and build up a statistical distribution of their deposition location. The accuracy of these predictions is, of course, dependent on the accuracy of both the CFD and the particle dynamics models.

Direct Navier–Stokes simulations of the flow field are precluded due to the extreme computational overhead involved, and laminar flow or Reynolds-averaged Navier–Stokes (RANS) modeling methods are generally used instead. Sarangapani and Wexler (2000) used a laminar flow model for nasal inspiration in a simplified anatomical geometry, together with a sophisticated particle dynamics model for particle sizes in the range 0.5–5 µm. This size range is the same order as many inhalation drug delivery systems. Yu et al. (1998) modeled the flow field in an anatomically realistic model of the entire extra-thoracic airway geometry (nasal and oral cavities, pharynx, trachea to past the first bifurcation) again using a laminar model, and investigated the deposition of ultrafine particles (<0.01 µm). Stapleton et al. (2000) used k–ε RANS modeling in an idealized representation of the oropharynx for oral inspiration of polydisperse particles with a mean diameter of around 5 µm. Li et al. (1996) also used a k–ε RANS model in a simplified representation of the mouth and throat, although they were investigating particle deaggregation rather than deposition. Other CFD studies of extra-thoracic airway flow did not involve deposition dynamics but concentrated exclusively on the fluid dynamics, often focusing on the flow field of the larynx and trachea, e.g., Renotte et al. (2000) and Katz and Martonen (1996), who both used k–ε RANS models in idealized geometries. The larynx/trachea region receives particular attention from CFD modelers as it is rich in fluid dynamics features, has a major influence on the fluid

A.F. Heenan, E. Matida, W.H. Finlay (✉)
Department of Mechanical Engineering,
University of Alberta, Edmonton, Alberta, Canada
E-mail: warren.finlay@ualberta.ca

A. Pollard
Department of Mechanical Engineering,
Queen's University at Kingston, Ontario, Canada

and deposition dynamics of the whole respiratory system, and its geometry lends itself to numerical modeling.

Typically, the accuracy of deposition predictors is investigated by comparing the results with experimental deposition measurements using gamma scintigraphy, gravimetry, spectroscopy, or other techniques. Yu et al. (1998) found "reasonable agreement" with experimental results for ultra-fine particle deposition at low flow rates. Stapleton et al. (2000) also had good deposition prediction for wholly laminar flow conditions (flow rate, $Q<2$ L/min), but found that significant errors develop at the onset of turbulence. However, turbulence will be present in many cases of practical interest, particularly during inhalation through drug delivery systems, where Q is generally high. Further development is therefore necessary before these methods become a robust tool for predicting deposition under these in vivo conditions.

However, there is a drawback with the above-mentioned validation approach: it does not decouple errors in the flow-field model from those in the particle dynamics model. This makes pinpointing the sources of error and their subsequent reduction or elimination more difficult. In order to decouple the errors, it is necessary to make both regional deposition measurements and an accurate experimental measurement of the flow field. This paper presents such a flow-field survey, in an idealized representation of the human oropharynx and modeling oral breathing through an inhaler mouthpiece (e.g., as would be used for aerosol drug delivery to the lung), and compares the results with various CFD models. Although the main motivation behind this work is the production of an experimental data set for validation of CFD models, the results in themselves provide a valuable insight into the structure and dynamics of human oropharynx (HOP) flow.

As well as making numerical modeling difficult, the complexity of the extra-thoracic airway flow field also poses serious challenges for experimental measurement, and relatively few such measurements are available in the literature. Much of the past experimental work has also concentrated on the larynx–trachea region (although Hahn et al. (1993) carried out hot-wire measurements in an anatomically correct 20 times scale model of the human nasal cavity). Corcoran and Chigier (2000) used phase Doppler interferometry to measure the flow field in a simplified model of the larynx–trachea, while Olson et al. (1973) present hot wire measurements in the larynx and trachea of an anatomically correct "average" oropharynx model. They found that the flow field in this region is dominated by the "laryngeal jet", a localized region of high-velocity fluid in the trachea downstream of the larynx, which is generated by the contraction associated with the glottis. The "jet" is surrounded by low-velocity or even reversed flow. The jet is also present in the CFD models of this flow field of Renotte et al. (2000) and Katz and Martonen (1996). Although several studies of the larynx–trachea flow field are present in the literature, to the authors' knowledge there has been no comprehensive experimental survey of the flow field across the entire HOP, i.e., from the lips to (and including) the trachea.

The three-dimensionality, turbulence and high spatial gradients make a comprehensive survey using point-measurement techniques such as hot-wire anemometry and laser Doppler velocimetry impractical, requiring thousands of individual measurements to resolve the flow. Particle image velocimetry (PIV), which simultaneously measures the velocity across a two-dimensional (2-D) plane, is a clear choice for this kind of survey. However, implementing PIV in a closed, complex, and small-scale geometry presents many practical difficulties. Two approaches to the problem are possible. The first is to use endoscopes to access the flow for imaging and also, possibly, for laser delivery. This method has been used successfully for making measurements inside turbomachinery (Wernet 2000) and internal combustion engines (Dierksheide et al. 2001; Nauwerck et al. 2000). Another approach, described in Hopkins et al. (2000), is to build a transparent model with an index-matched working fluid and use standard PIV imaging and laser delivery systems. For the present work, which establishes the first comprehensive survey of the flow field across a whole HOP geometry, it was decided to use endoscopic PIV, because endoscopic PIV is somewhat more established and issues relating to its implementation are better covered in the literature.

2
Experimental method (model geometry and manufacture)

The geometry of the HOP is rather poorly defined. Not only is there huge intersubject variability, but the geometry also varies with time within a given subject. In the present work, experiments were carried out in an idealized geometry, which represents an "average" HOP when breathing from a circular mouthpiece (an idealized inhalation device). A sagittal view of the geometry together with several cross-sections is shown in Fig. 1. The geometry is built up of simple geometric shapes but possesses all the basic anatomical features of a real HOP. The design is a slight variation of the one described in Stapleton et al. (2000), which was developed based on information from MRI and CT scans, direct observation of living subjects and data in the archival literature. The rationale behind the geometry and choice of dimensions are fully detailed in that paper. The variation in cross-sectional area with distance distal from the mouth of the present geometry compares quite well with that of an "average" oropharynx described in Olson et al. (1973), with a maximum cross-sectional area in the oral cavity of about 14 cm^2, and cross-sectional areas of the pharynx, larynx (glottis), and trachea of about 2.4, 1.0, and 2.0 cm^2 respectively. The present glottal area value is very close to the 0.98 cm^2 quoted in Brancatisano et al. (1983) for the average area of the glottal opening during normal breathing. Katz and Martonen (1996) also represented the trachea as a circular cylinder, albeit with a diameter of 18 mm as opposed to 16 mm in the present model. DeHaan and Finlay (2001) measured total deposition with a straight tube inlet in the present geometry. Their results compared very well with in vivo measurements and the empirical model of Stahlhofen et al. (1989).

It was decided to use a double-scale model for the PIV experiments, primarily because it doubled the effective accuracy in setting-up and aligning the endoscope and
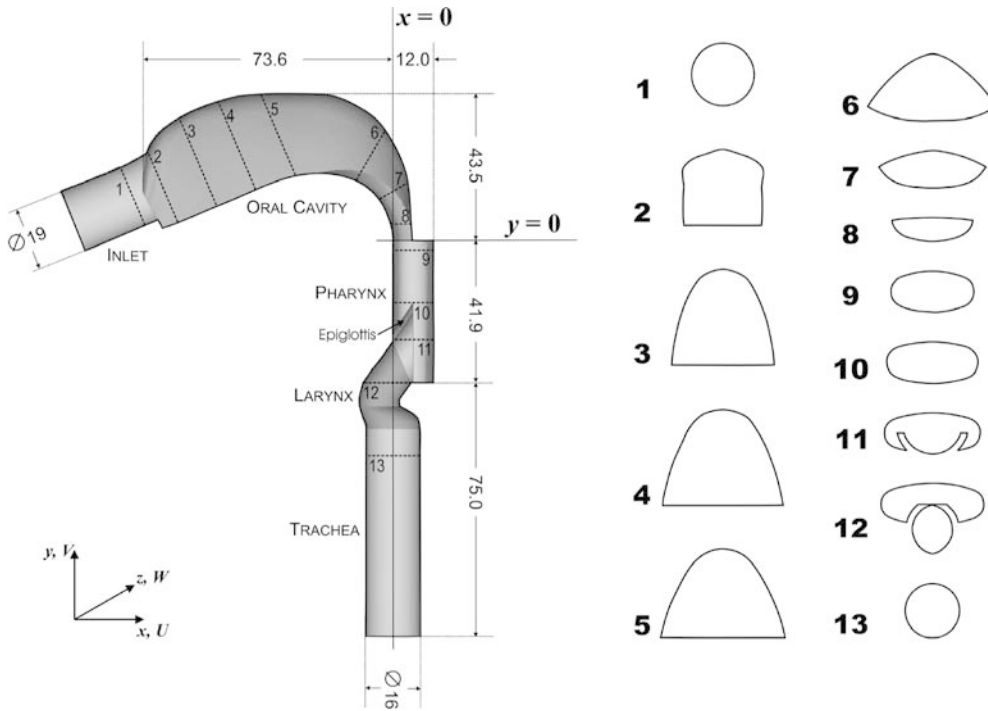
Fig. 1. Idealized model geometry with coordinate and naming conventions

laser sheet. The larger model was also easier to manufacture, prepare, and work with. Finally, doubling the distance between the endoscope and laser sheet allowed a more accurate correction for the "fish-eye" distortion of the endoscope image. The flow rate through the double-scale model must be doubled in order to maintain the full-scale Reynolds number. Apart from the physical discussion of the model in this section, all dimensions, flow rates etc. mentioned in the text have been scaled to full-scale geometry values.

A three-dimensional (3-D) CAD model of the geometry was designed using ProEngineer (PTC, Needham, Mass.) and DeskArtes 3Data Expert (DeskArtes Oy, Helsinki, Finland) software packages. The model was designed in two halves with the split offset from the central plane by 7.5 mm. The model walls were approximately 6 mm thick. Included in the design were slots for laser windows, and appendages for bolting the two halves of the model together and for mounting the model to the rest of the experimental apparatus (part of the model can be seen in Fig. 3). The models were manufactured using a Stratasys FDM 8000 rapid-prototyping (RP) system (Stratasys Inc., Eden Prairie, Minn.). This uses a fused deposition modeling process to build the models in ABS plastic. After manufacture, the inside surfaces of the models were repeatedly brushed with dichloromethane to smooth out "steps" in the curved surfaces, which were artifacts of the RP process. This solvent liquefies the plastic at the surface of the model, which then flows slightly before resolidifying as the solvent evaporates. The models were then coated with epoxy sealant and finally painted with a thermally resistant paint. Matte black was used to minimize laser reflections.

The endoscope was always oriented perpendicular to the x–y plane (see Fig. 1) to minimize optical distortion. Its working distance ranged from approximately 10 to

40 mm, and only a small portion of the central plane could be imaged at a time. To cover the entire plane, it was necessary to make measurements at 27 separate locations. Holes that were not in use were sealed with wax. Four 5-mm-wide windows located on the central x–y plane allowed laser illumination of practically any region of the plane. Fused silica glass 1.5 mm thick with a broadband antireflective coating was used for straight windows, while 3-mm-thick Pyrex was used for curved ones. The windows were sealed in place using Dow Corning 734 flow-able sealant (Dow Corning Corporation, Midland, Mich.). Although the surfaces where the windows were located were generally curved in the z direction, the radii of curvature were sufficiently large that the inclusion of "flat" windows caused a negligible change in the local geometry.

2.1
Experimental setup

Figure 2 shows a schematic of the experimental apparatus, and Fig. 3 illustrates how PIV was implemented in the model. A volume of seeded fluid was prepared immediately before each measurement and stored in a reservoir bellows with a maximum capacity of 200 L. A pipe 800 mm long, with an inner diameter of 100 mm, followed by a nozzle with a 7:1 diameter contraction ratio, connected the reservoir to the model. A butterfly valve seale the reservoir from the model when the reservoir was being filled. The open butterfly valve was about 4.5 mm wide and created a blockage of about 6% in the tube connecting the reservoir to the model. Hot-wire measurements made just downstream of the inlet to the oral cavity, with and without the (open) butterfly valve in place, showed that the presence of the open butterfly valve had a minimal effect on inlet flow conditions. Particles were generated using a TSI Model 3475 Aerosol Generator (TSI Incorporated, St Paul, Minn.), which produces
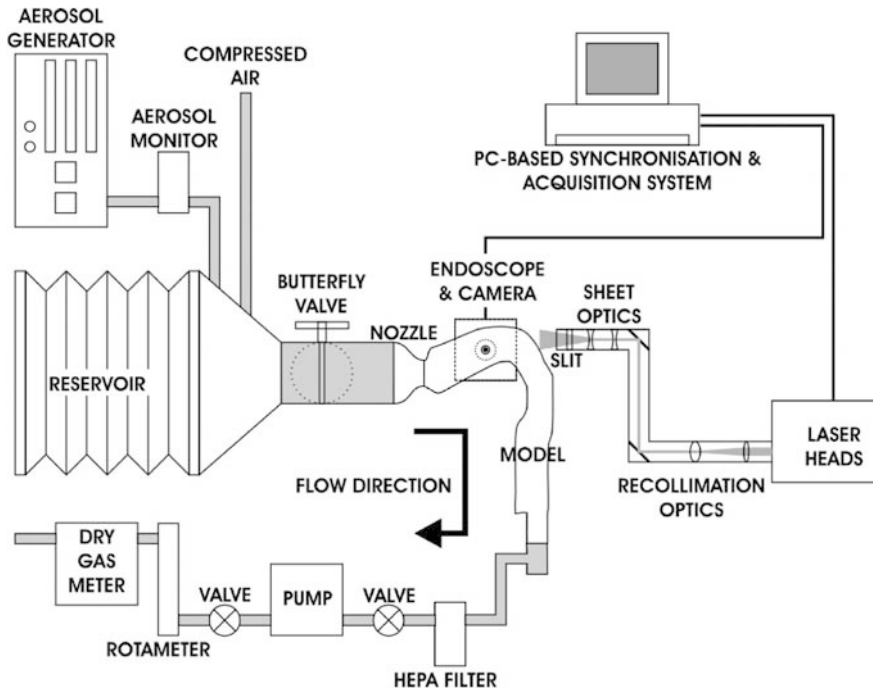
Fig. 2. Experimental apparatus schematic

monodisperse (geometric standard deviation, $\sigma=1.1$) di-2-ethylhexyl-sebacate (DEHS) particles with a NaCl nucleus. The size of the particles exiting the generator was monitored using a TSI 3375 Process Aerosol Monitor. Typically, the particles used had a mean diameter of 1.7–2.4 µm. The generator's output was diluted with air to the desired concentration level, which varied between 50 and 300/mm^3, depending on the magnification of the endoscope image. A throttled regenerative blower sucked the fluid through the model. Measurements were made at flow rates of 30, 60, and 180 L/min, which correspond to flow rates of 15, 30, and 90 L/min full scale. A rotameter was used to set the flow rate to the desired nominal value for each experiment, and the actual volume flow rate during the experiment was measured using a Singer DTM 115 dry gas meter.

2.1.1
Illumination

A Spectra-Physics PIV 400 laser system (Spectra-Physics Inc., Mountain View, Calif.) provided illumination of the particles. This system consists of a pair of Nd:YAG lasers, producing 5–10 ns pulses with energies of up to 400 mJ/pulse and a 10 Hz repetition rate. In the present experiments, only energies of 10–20 mJ/pulse were used. Using two lasers allowed arbitrarily short time intervals between pulses. The heads were housed in a single enclosure, where the beams were made collinear and frequency doubled. Upon exiting the laser enclosure, the lasers were re-collimated from their nominal beam diameter of 9 mm to about 3 mm using a pair of plano-convex lenses. Three 532-nm mirrors steered the beams to the model. After the second mirror, a pair of cylindrical mirrors spread the beams into a sheet, which then passed through a thin (either 0.5 or 1.0 mm wide) slit aligned with the plane of the sheet. The final mirror directed the sheet into the model. As only the central third or so of the laser sheet
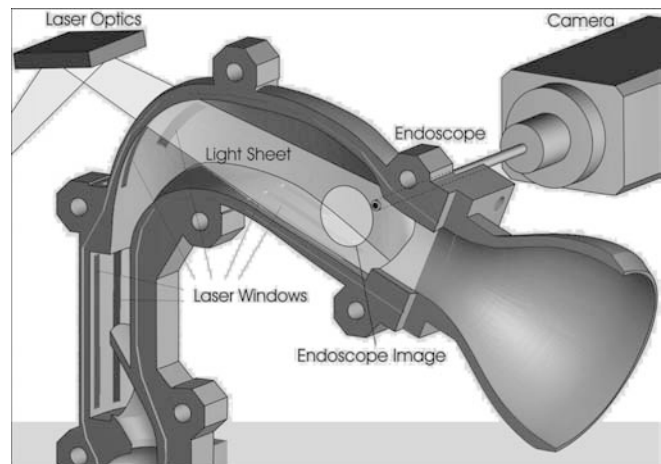

Fig. 3. PIV implementation schematic

passed through the slit, the variation in light intensity across the thickness of the sheet within the model was reduced, and resulted in a more uniform brightness of the imaged particles.

2.1.2
Imaging

The particle images were recorded using a LaVision FlowMaster 3 digital camera (LaVision GmbH, Goettingen, Germany). The camera's 2/3-in. format CCD sensor has a resolution of 1,280×1,024 pixels and a 12-bit dynamic range, and was equipped with a 532-nm line filter to minimize stray light. It captured image pairs at an average rate of approximately 2–3 Hz. The endoscope was designed and manufactured specifically for these experiments by GriNext (St Petersburg, Russia). It has a 5-mm outer diameter with single 4-mm diameter gradient-index rod lens running the whole length of the scope. The

endoscope was coupled to the camera via an adaptor, which provided focus and zoom. The resolution of the endoscope system was measured at approximately 80 line pairs/mm on the 8.5×6.9 mm CCD sensor. A PC-based PIV synchronization and acquisition system from LaVision was used to control the laser and camera.

3
PIV measurement and analysis

The measurements at each endoscope location represent an essentially independent experiment. Once the camera–endocscope system and laser sheet had been set up and aligned for a particular endoscope location, the working distance between the endoscope and image plane was measured, and the endoscopic image distortion was calibrated for that distance. Then, a series of preliminary PIV measurements were carried out over a wide range of Δt and laser powers to determine the optimum values. The optimum Δt was considered to be the longest interval for which "most" (arbitrarily determined by inspection) of the measured vector field was spurious-vector free. Δt varied from 1,000 μs to 10 μs. A measurement consisted of 100 image pairs at 15 and 30 L/min and 80 image pairs at 90 L/min. The number of images that could be captured at 90 L/min was limited by the volume of the reservoir. A second measurement was also carried out at approximately (0.7–0.5) Δt, in case the results for the optimum Δt were subsequently found to be noisy. This second measurement sacrificed some dynamic velocity range and accuracy for an improved signal-to-noise ratio. Generally, the results for the two Δt values were very similar and the longer interval data were used in these cases.

The image data were analyzed using the DaVis 6 software package from LaVision. The vector fields were generated using cross-correlation fast Fourier transform (FFT) with an adaptive multi-pass procedure based on Scarano and Reithmuller (1999). The interrogation region decreased from 128×128 to 64×64, and then to 32×32 pixels on each pass, with an overlap of 50% on the final pass. After each intermediate iteration, the vector field was filtered for spurious vectors using velocity range, peak ratio (1.5), and local median filters. A more sophisticated post-processing routine is applied after the final pass. It is similar to the procedure described in Nogueira et al. (1997), which is based on how the human mind appears to validate vectors in a vector field. The philosophy is to first establish regions of the vector field where there is a very high probability of all the vectors being valid, by aggressively removing any remotely suspicious vectors. After these regions have been established, previously deleted vectors that are consistent with the "valid" vector field are then replaced. A velocity range and peak ratio filter is first applied to the data in the procedure used. Vectors deleted by these filters cannot be replaced. A local median filter (two standard deviations) followed by a number-of-neighbors filter (three) were used to establish the valid vector regions. Deleted vectors were now replaced if they had at least three valid neighbors and were within 2.5 standard deviations of the median of these neighbors. If a deleted vector was not accepted for reinsertion, vectors corresponding to the 2nd, 3rd, and 4th

peaks in its cross-correlation map were also checked, although these vectors are very rarely chosen. This reinsertion process was iterated until no more vectors could be replaced. Finally, any group of less than four vectors was removed. This procedure gives a vector field with few spurious vectors, at the expense of some valid ones. The entire data set (>10^4 images) was also analyzed using a four-stage multi-pass algorithm, from 128×128 to 16×16 pixels with no overlap. However, it was found that the gains in spatial resolution were offset by a generally lower signal-to-noise ratio (see below).

3.1
Discussion of experimental errors (setup)

In order to survey accurately the whole flow field, it was necessary to repeat a careful setup and calibration procedure at each of the 27 endoscope locations. Inaccurate positioning or alignment of the endoscope, laser, calibration plate or model introduces a systematic error into the measurements for that location. Assessment of this error was done in two ways. The first was in the raw images. The laser sheet produces a bright well-defined line anywhere it makes contact with the surface of the model. This provides precise "reference points" within the image. The location of these reference points deviates from their nominal positions if any positional and/or alignment errors are made while setting up. Analysis of the images indicated that, on average, the reference points deviated from their nominal positions by approximately 1.8% of the working distance (the average working distance was approximately 23 mm). This value is an estimate of the level of measurement error introduced during setup. The second assessment was from the velocity-field contour plots. As the vector field from each endoscope location is an independent measurement, the alignment of results in overlap locations is another indication of the level of setup error present. In the regions where the results from multiple endoscope locations overlap, the measurements generally agree to within a few per cent. This is evidenced by the excellent alignment of the contour lines from different endoscope locations.

Uncertainty in flow rate measurement, which would also affect the matching up of the contour plots, was measured at less than 0.5% for 15 and 30 L/min measurements and less than 1% for 90 L/min. During a measurement, there was a slight monotonic decrease in the instantaneous flow rate, due to the increased resistance presented by the reservoir bellows as it was compressed. The flow rate variation was measured at about 0.5% per 100 L decrease in volume. Although this would have a negligible effect on the mean results, it would introduce a small positive bias on the turbulence intensity levels: approximately 0.05%, 0.09%, and 0.26% for the 15, 30, and 90 L/min experiments respectively.

3.1.1
Endoscopic imaging

The wide angle of view of the endoscope means that velocity measurements far from the optical axis are contaminated by particle image displacement due to the out-of-plane velocity component. For this reason,

measurements were limited to the $z=0$ plane where, by symmetry, the mean out-of-plane velocity should be small and the in-plane velocity components should dominate the instantaneous velocity field. The z component biases the in-plane measurement either towards or away from the center of the endoscope image, depending on whether the out-of-plane motion is away from or towards the endoscope. Therefore, where two endoscope images overlap, a finite z component biases the results of the two images in roughly opposite directions (i.e., either both toward or both away from their respective centers). The generally excellent matching up of the edges of individual contour plots and smooth streaklines confirms the small magnitude of the mean z component and any resulting errors. The endoscope image has a wide angle of view ($>60°$) and is subject to a "fish-eye" distortion, where, at the edge of the image, the magnification is reduced as displacements in the light sheet plane are projected onto a plane perpendicular to the viewing angle. The variation in magnification across the image for the present system was approximately 15%. This distortion was measured immediately before measurements by imaging a calibration plate, displaying an orthogonal grid of equally spaced crosses, placed at the working distance. The image was analyzed using a routine in DaVis 6, which detects the crosses and calculates the mapping function required to transform the distorted image back to the original orthogonal grid. After correction, the variation in magnification across the image was approximately 1%. Several calibration plates were used in order to maintain the optimum number of crosses in the calibration image for the 10–40 mm working-distance range. For the shorter working distances, the uncertainty in the location of the crosses was of order 1%. This procedure also serves as a magnification calibration, as the distance between the crosses is known. During analysis, the correction transformation is applied to the final vector fields rather than raw images as this requires less computational effort.

The relatively low ratio of working distance to laser sheet thickness in these measurements results in a variation in the magnification of individual particle displacements, depending on their location across the thickness of the laser sheet. The laser slit width was 1.0 mm for working distances above 20 mm, and 0.5 mm for working distances below 20 mm. Thus, the variation in magnification was always below ±2.5%. The effect on the cross-correlation is the same as would be produced by a uniform out-of-plane velocity gradient and probably has a similar effect as an in-plane velocity gradient, which is to broaden and flatten the displacement correlation peak. From the estimation of measurement uncertainty due to in-plane velocity gradients given in Raffel et al. (1998, p. 145), it is estimated that the effect causes an increase of less than 0.1 pixel in the uncertainty in the displacement estimation. Also, the contribution to the correlation from the particles that are closer to the endoscope is slightly greater, as these particles have a brighter image. Therefore, the correlation is slightly biased towards higher displacements. For the present experiments, however, this bias is estimated to be less than 0.1% of the local displacement in the worst case and is therefore ignored. The variation in magnification

causes another, but negative, displacement bias. This is due to a higher rate of in-plane loss-of-pairs towards the front of the laser sheet, due to the increased image displacement. This effect is considered negligible.

It is difficult to achieve a sharp focus over the whole of the endoscope image (Dierksheide et al. 2001). This is because the surface of focus at the object is not planar. In these experiments, the object was focused at the optical axis, which leaves the edges of the image slightly out of focus. This does not preclude PIV analyses at the edges of the image, but it does increase the uncertainty in the correlation peak location and lower the signal-to-noise ratio as the light from individual particles is spread over a wider area. Less light is received from these particles in any case, further reducing signal-to-noise ratio. Although it is difficult to quantitatively assess the errors associated with this problem, the effect was visible in the results, with those data towards the edge of the image becoming increasingly noisy (showing negative bias in mean velocity measurements and positive bias in turbulence intensities). Fluctuations in the z component also positively bias turbulence intensity measurements at the edge of the image. Inspection of the results indicated that, in general, the mean flow measurements were consistent over the central 90% or so of the image. Turbulence intensity measurements are much more sensitive to experimental noise, and only the central 80% of the image produced satisfactory results. The data presented here are masked to show only these regions.

3.1.2
Frequency response and spatial resolution
The frequency response of the measurements is limited by two factors: the spatial resolution of the PIV analysis, which is determined by the size of the interrogation region, and the flow tracking ability of the seeding particles. Melling (1997) provides a useful estimate for the frequency response of seeding particles in the form of an expression for the ratio of the kinetic energy of the particle velocity fluctuations to the fluid turbulent kinetic energy in terms of the particle properties and "the highest turbulence frequency of interest" in the flow, f_c. It is likely that the separated shear layer formed downstream of the sudden expansion at the start of the pharynx contains some of the smallest scales and highest frequencies in the present flow field. From available backward-facing-step spectra, a reasonable estimate for f_c is 10 U_s/h_s, where h_s and U_s are the height of the "step" and the free-stream velocity at the sudden expansion. This gives f_c values of about 1,000, 2,000, and 6,000 Hz for the 15, 30, and 90 L/min experiments respectively. These f_c values relate to the actual experimental conditions, which is double scale. They would be four times higher in a full-scale model. Melling's expression gives kinetic energy ratios of about 95%, 90%, and 75% respectively for 2-μm DEHS particles. Therefore, the imperfect flow tracking ability of the particles used in the experiments causes significant underestimations of fluid turbulence kinetic energy in localized regions of the flow at the highest flow rate. Experiments with smaller particles (~1 μm) were attempted, but the increase in laser power required to
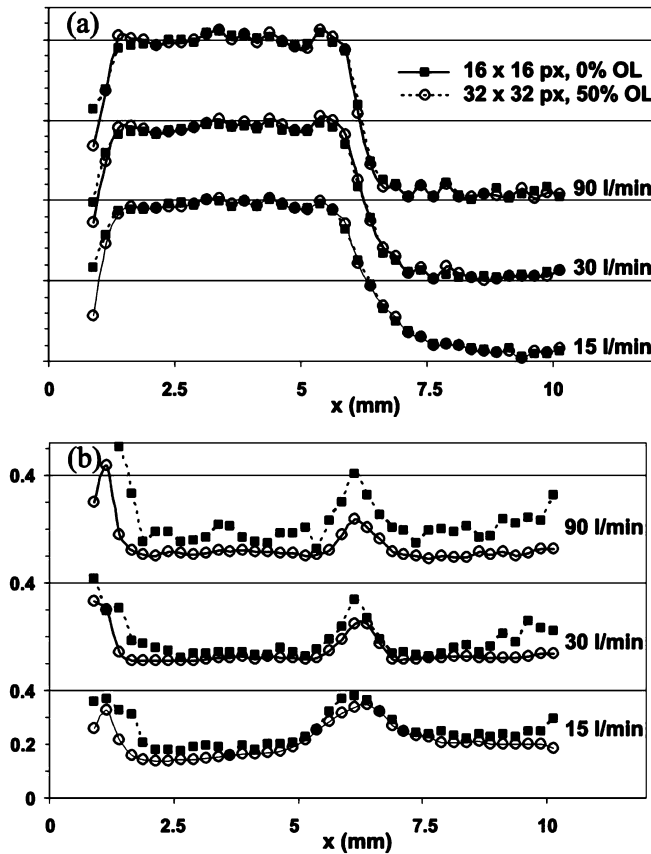
Fig. 4a, b. Effect of final interrogation region size on PIV measurements in the pharynx at $y=-2.5$ mm: **a** velocity magnitude normalized by velocity magnitude at the sudden expansion; **b** turbulence intensity normalized by velocity magnitude at the sudden expansion

illuminate them resulted in so much glare from the walls of the model that the images became very noisy.

The smallest turbulent fluctuations that PIV analysis can resolve are on the scale of the size the interrogation region, l, which averages about 0.9×0.9 mm for a 32×32 pixel interrogation region. This corresponds to a frequency resolution of order U/l, where U is the local fluid velocity. At 15 and 30 L/min, this is the primary factor limiting resolution. The effects of finite spatial resolution were investigated by comparing the 32×32, 50% overlap measurements with results using a 16×16 pixel final pass (doubling the spatial resolution at the expense of signal-to-noise ratio). Figure 4 displays mean velocity and turbulence intensity profiles in the pharynx at $y\approx-2.5$ mm (about $0.4h_s$ downstream of the sudden expansion). This location was chosen as spatial scales will be among the smallest and spatial gradients among the highest of the entire flow field. These data were normalized using the average velocity magnitude at the sudden expansion. The mean velocity profiles agree very well: the 32×32 profiles are not affected by the high velocity gradients, which can cause a bias toward lower velocities (Keane and Adrian 1992). Agreement for the turbulence intensity profiles is also generally good, although, as the flow rate increases, the 32×32 analysis does increasingly underestimate the turbulence intensity peak in the center of the shear layer.

This is due to a combination of spatial "smoothing" of the narrow intensity peak and the under-resolution of the smallest flow scales. Measurements near $x=0$ are affected by noise caused by glare from the wall (at $x=0$), with both analyses overestimating turbulence intensity levels.

3.1.3
PIV analysis
A combination of numerical effects and image parameters influence the uncertainty and systematic error in the displacement estimation for a given interrogation region using a cross-correlation FFT. The magnitudes of bias and uncertainty increase as the displacement correlation peak moves from the center to the edges of the correlation domain (Keane and Adrian 1992). The adaptive multi-pass procedure reduces systematic error and uncertainty by placing the displacement correlation peak very close to the center of the cross-correlation domain. In the central 80% of the endoscope images, typical interrogation region parameters were as follows:

1. Number of particles: 10–40
2. Diameter of particles: 3–4 pixels
3. Average particle displacement: 10–15 pixels

Using the analyses presented in Raffel et al. (1998), it is estimated that for these parameters the uncertainty in locating the center of the displacement peak is around 0.1 pixels, which is of order 1% of the average displacement, and that the likelihood of detecting the correct peak approaches unity. No significant systematic error is expected. Inspection of vector histograms showed no evidence of peak-locking. These estimates only apply where the image quality is high. Errors are significantly higher at the edges of the images and also near walls, where the particle images are contaminated by laser glare.

3.1.4
Statistical uncertainty
There is a statistical uncertainty present in the time-averaged quantities due to the finite number of measurements used in their calculation. The flow in the mouth, pharynx, and trachea are each made up of regions of low and high turbulence. At a 95% confidence level, statistical uncertainty in mean velocity and turbulence intensity is around 1% of the local maximum velocity in regions where turbulence is low, and up to about 5% of the local maximum velocity where turbulence is high. Uncertainty levels are higher at the edges of the images because fewer valid vectors are generally accepted when evaluating the statistic. As well, there is a greater probability that an invalid vector is included in the estimation.

3.1.5
Experimental conditions
If the flow continued to develop during a measurement, then ensemble averages of the vector fields from the first 50% of image pairs of that measurement should be significantly different than the average of the last 50%. These two ensemble averages were compared for several measurements at all flow rates and showed no evidence that the flow was not fully developed during measurements.

Table 1. Test and scaled experimental parameters

	Test				Scaled			
	Flow rate (L/min)	Re	U_{inlet} (m/s)	Inlet dia. (mm)	Flow rate (L/min)	Re	U_{inlet} (m/s)	Inlet dia. (mm)
	30	1,100	0.44	38	15	1,100	0.88	19
	60	2,200	0.88	38	30	2,200	1.76	19
	180	6,600	2.64	38	90	6,600	5.28	19

There were no consistent trends in the difference between the two ensemble averages. The magnitudes of the differences were those expected due to statistical uncertainty. The differences were the same magnitude for all flow rates and, for the lower flow rates, were not affected by running the flow for up to a minute before starting the measurement.

4
Computational model
The incompressible, steady form of the governing equations (Navier–Stokes and mass conservation) were solved using CFX-Tascflow (version 2.11, AEA Technology Engineering Software). An IGES (Initial Graphics Exchange Specification) file of the mouth–throat geometry was imported. Structured grids over two domains were used. One domain consisted of the geometry described in Sect. 2. The second domain included the first with the addition upstream to the oral cavity inlet of a cylinder 50 mm in diameter and 250 mm long followed by a 7:1 contraction ratio nozzle, which is a more accurate representation of the experimental setup (see Fig. 2). Both grids contain approximately 1,050,000 hexahedric elements, with biased accumulation of nodes towards the wall. Analysis of results from using four different grid sizes (approximately 260,000, 450,000, 710,000, and 1,050,000 hexahedric elements) indicates that the results obtained are independent of grid resolution, at least with respect to mean quantities. The grid densities considered far exceed those reported in any other human extra-thoracic airway modeling effort. A modified, linear profile scheme is used to discretize the convection terms; while this is not formally second-order accurate, it gives adequate results in a robust manner, which is particularly relevant here.

Both laminar and turbulent solutions were obtained. In the case of turbulence, the standard k–ω turbulence model (Wilcox 1988) with the Kato and Launder (1993) modification and near-wall treatment for low-Reynolds number based on Grotjans and Menter (1998) was employed. A broad range of different model types were tested, such as the standard k–ω model, the shear stress transport (SST) k–ω turbulence model of Menter (1994), the algebraic stress model (ASM) of Speziale and Gatski (1993), and the Reynolds stress model (RSM) of Speziale–Sarkar–Gatski, but none of them gave better results concerning the viscous effect discussed later. Indeed, Heyerichs and Pollard (1996) found the k–ω turbulence model best for wall bounded flows, especially for cases where there are regions of favorable and adverse pressure gradients, which are expected in the flow considered.

Three inlet boundary conditions were tested: inlet plug flows (i.e., "top hat" velocity profiles) for the two grids (i.e., with and without the inlet nozzle and upstream tube), and an inlet velocity profile based on the PIV measurements at the inlet. For turbulence boundary conditions, a turbulence intensity of 5% of the mean velocity and a turbulence length scale of 10% of the inlet diameter were prescribed at the inlet. Varying the turbulence boundary conditions had little effect on the final results. Each calculation required approximately 20 CPU hours on an Athlon 1.4 GHz PC.

5
Results (global flow structure)
Table 1 presents test and scaled experimental parameters for the three flow rates. U_{inlet} is the inlet plug-flow velocity. The Reynolds numbers are based on inlet diameter and U_{inlet}.

The experimentally measured, normalized contours of mean velocity magnitude for 30 L/min are presented in Fig. 5. Velocity magnitude is a scalar, always positive and has been normalized against U_{inlet}. Figure 6 shows streaklines computed from the same 2-D velocity field. A streakline represents the path a massless particle would follow in the 2-D velocity field described by the PIV measurements.
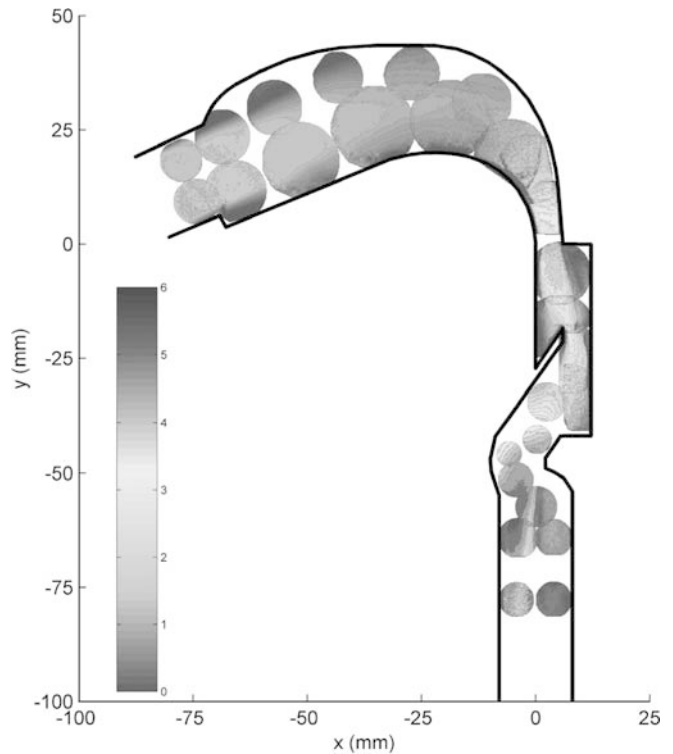
Fig. 5. Time-averaged velocity magnitude from PIV with an inhalation flow rate of 30 L/min, normalized by the inlet plug-flow velocity
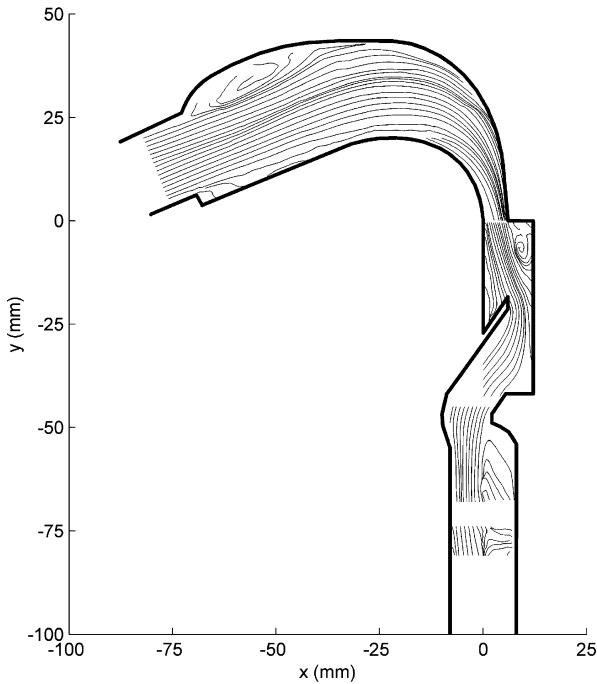
Fig. 6. 2-D streaklines from PIV with an inhalation flow rate of 30 L/min

The flow is characterized by three major regions of separated flow at the start of each of the oral cavity, pharynx, and trachea respectively. A separation bubble forms in the roof of the mouth due to the sudden change in geometry from inlet orifice to oral cavity. It has a mean reattachment length of about 40 mm. The instantaneous vector fields show that the structure of the bubble varies considerably in time. It was not possible to determine instantaneous reattachment points from the PIV data. However, the y position of the shear layer can vary by over 5 mm, and it is likely that the instantaneous reattachment length varies by several times this value. The instantaneous thickness of the separated shear layer was of order 2 mm and coherent vortical structures were evident.

Downstream of the separation region the flow accelerates to over $3U_{inlet}$ due to the contracting cross-sectional area, before passing through the sudden expansion at the start of the pharynx. The mean reattachment length of the pharynx separation region is about $2h_s$ (where h_s is the height of the step at the start of the pharynx). This is much shorter than that typically quoted for backward-facing step flow (about 5–$7h_s$), and is due to the constriction imposed on the flow by the epiglottis on the anterior (front) wall. Figure 7 is an instantaneous vector plot from the upstream end of the pharynx (the region between cross-sections 8 and 10 in Fig. 1), and illustrates the highly turbulent nature of the flow. To show the location of the walls, a "negative" of the endoscope image is included as a background. Two large (2–3-mm diameter) vortices can be seen in the separated shear layer. Inspection of several vector plots showed that the instantaneous size and shape of this separation bubble also varied considerably in time.

The highest velocities in the flow field ($>4U_{inlet}$) are achieved at the entrance to the trachea. This acceleration is caused by the small cross-sectional area of the larynx,

which is further constricted by a separation bubble formed from the tip of the epiglottis. This high-speed fluid, the "laryngeal jet", enters the trachea at an angle, impinging against and flowing along the anterior wall of the trachea. This induces a highly 3-D recirculation region (discussed further below) in the posterior half of the trachea which extends downstream beyond the limit of measurements. Interestingly, in many investigations of larynx/trachea flow the laryngeal jet is described as flowing along the posterior wall with the separation region close to the anterior wall, e. g., Corcoran and Chigier (2000), Renotte et al. (2000) and Olson et al. (1973) although, in the model of Katz and Martonen (1996), the jet is down the center of the trachea. The variation in location of the jet is due to the different cross-sectional shapes used to model the glottis and the variation in the inclination of the jet to the long axis of the trachea.

Figure 8 is the measured turbulence intensity field, $\frac{\left(\overline{u^2}+\overline{v^2}\right)^{1/2}}{U_{inlet}}$ for 30 L/min. Not surprisingly, turbulence intensities are at their lowest at the upstream end of the oral cavity. Overall turbulence intensity levels in the oral cavity are relatively low. Downstream of the oral cavity, there is a general increase in turbulence intensity levels, corresponding to the increases in mean velocity. The highest turbulence intensities are found in the separated shear layers in the pharynx and trachea.

5.1
Three-dimensionality

The streaklines in Fig. 6 appear to "violate" 2-D continuity at several locations, which indicates the presence of 3-D flow. The streaklines at the end of the oral cavity just upstream of the pharynx are clustered close to the posterior wall. They are driven to the posterior wall by a local counter-rotating secondary motion, where fluid close to the central plane of symmetry flows from anterior to posterior and then around the walls from the posterior to the anterior side. This secondary flow is a Dean flow, caused by the strong curvature of the local geometry. The Dean number, $\kappa = \left(\frac{\sqrt{A_{local}}}{2R}\right)^{1/2}\frac{Q}{v\sqrt{A_{local}}}$ (where A_{local} is the local cross-sectional area), is high, of order 10^3 at 30 L/min, and secondary motion develops very soon after the onset of curvature (Berger et al. 1983). Three-dimensionality is also seen with streaklines impinging upon the upstream face of the epiglottis, which suggests that a large proportion of fluid flows around the sides of the epiglottis rather than over it. However, the instantaneous vector plots sometimes showed a recirculation region just upstream of the epiglottis.

The recirculation region in the trachea appears to be highly 3-D, unlike the other major recirculation regions. It also involves a counter-rotating secondary flow, where fluid from the impinging laryngeal jet flows along the walls from the anterior to posterior side and then flows from posterior to anterior around the central plane. Renotte et al. (2000) describe a similar counter-rotating secondary motion in their CFD simulation of larynx–trachea flow, albeit counter-rotating in the opposite direction, due to the
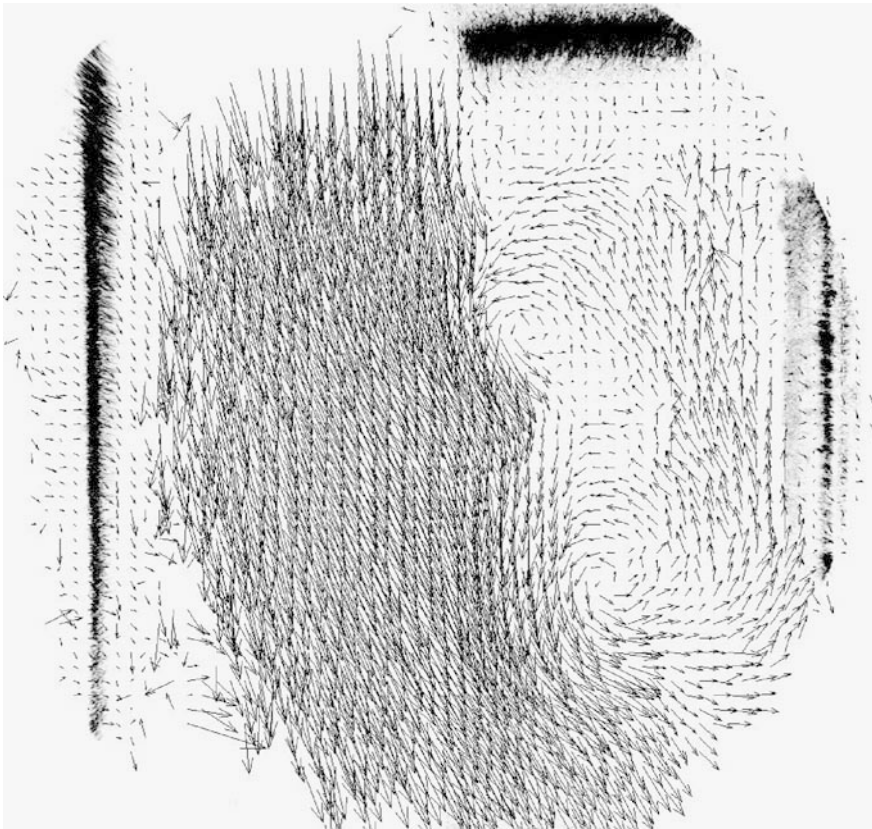
Fig. 7. Instantaneous velocity measurement from PIV in the upper pharynx (between cross-sections 8 and 10 in Fig. 1) at an inhalation flow rate of 30 L/min
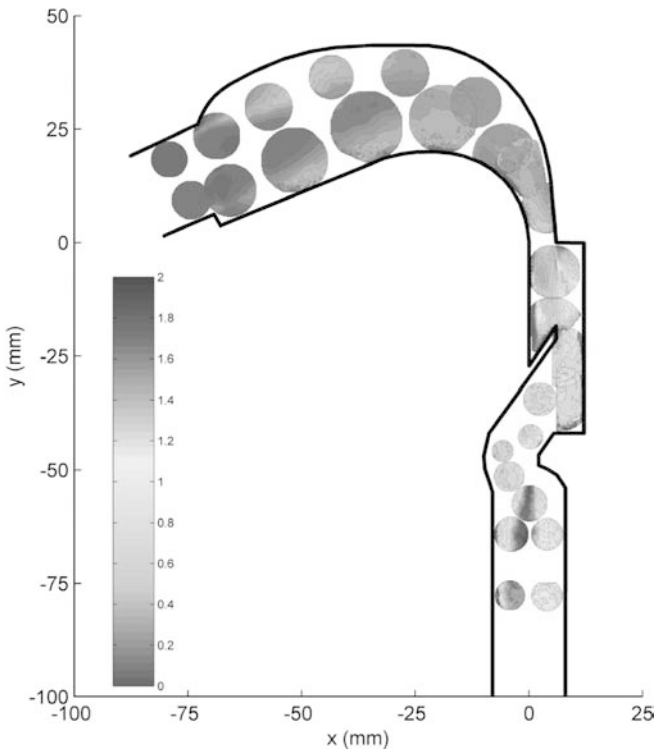

Fig. 8. Normalized RMS velocity, $\frac{\left(\overline{u'^2}+\overline{v'^2}\right)^{1/2}}{U_{\mathrm{inlet}}}$, from PIV with an inhalation flow rate of 30 L/min

fact that in their results the laryngeal jet and separation region are on the opposite sides of the trachea to those in the present work. Admittedly, the evidence for all these

3-D motions is only indirect in the PIV measurements. However, all the motions described above are clearly evident in the present CFD results.

5.2
Effect of Reynolds number

Figures 9 and 10 are the average velocity magnitude and streakline plots for 15 and 90 L/min, respectively. The streakline plots are quite similar for all three flow rates, indicating an essentially similar flow structure across the range of Reynolds numbers. However, there are some minor structural variations with increasing Reynolds number that are worth noting. The pharyngeal separation bubble becomes somewhat longer; the laryngeal jet becomes slightly thinner; and the curvature of the streaklines around the epiglottis becomes more pronounced.

The primary effect of changing Reynolds number can be seen in the velocity magnitude contour plots of Figs. 5, 9, and 10. The non-dimensionalized core velocities of the "jets" entering the oral cavity, pharynx and trachea, increase appreciably as Re decreases. This is caused by the stronger viscous effects, which increasingly retard fluid motion close to the wall. This results in the core fluid moving faster in order to maintain the overall flow rate. Interestingly, the effect is not limited to the downstream regions of the model but is also present to some extent near the inlet. This indicates that there has been appreciable flow development in the pipe connecting the reservoir to the inlet nozzle. Although this pipe is relatively short, with a length to diameter ratio of around 5, the pipe Reynolds number is so low at low flow rates ($Re \approx 450$ at
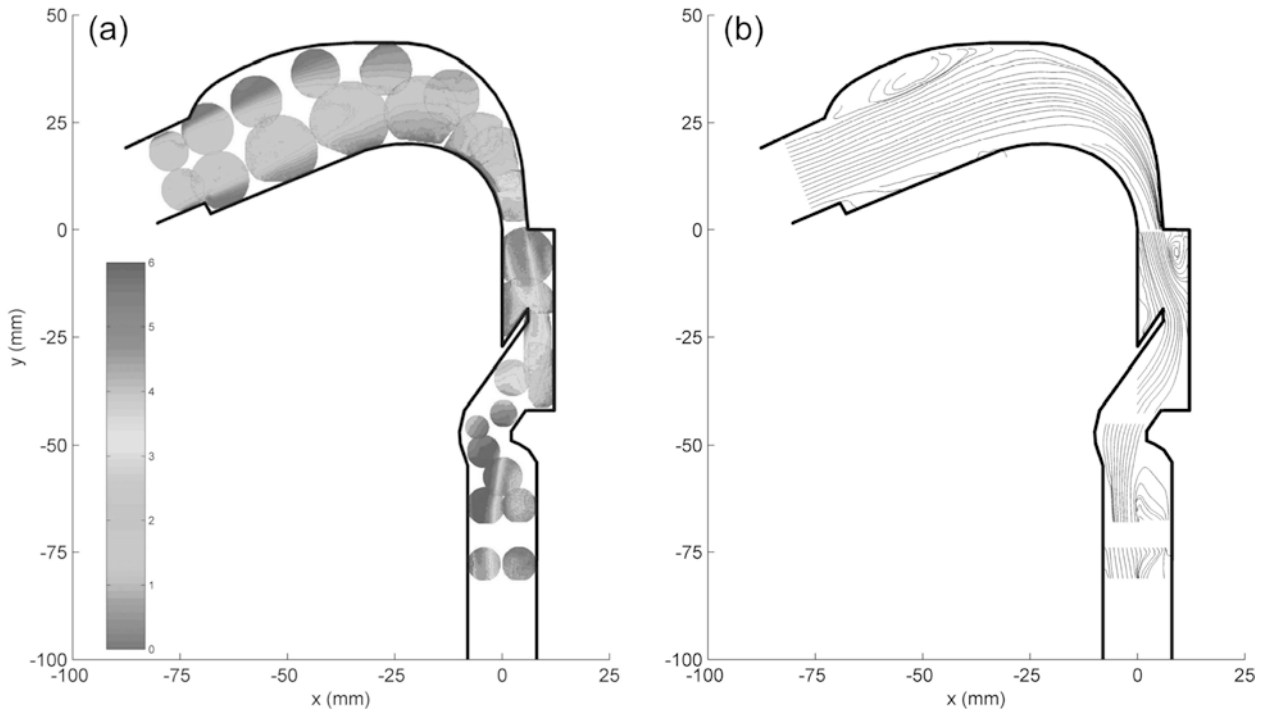
Fig. 9. Time-averaged measurements from PIV with an inhalation flow rate of 15 L/min: **a** time-averaged velocity magnitude normalized by the inlet plug-flow velocity; **b** 2-D streaklines
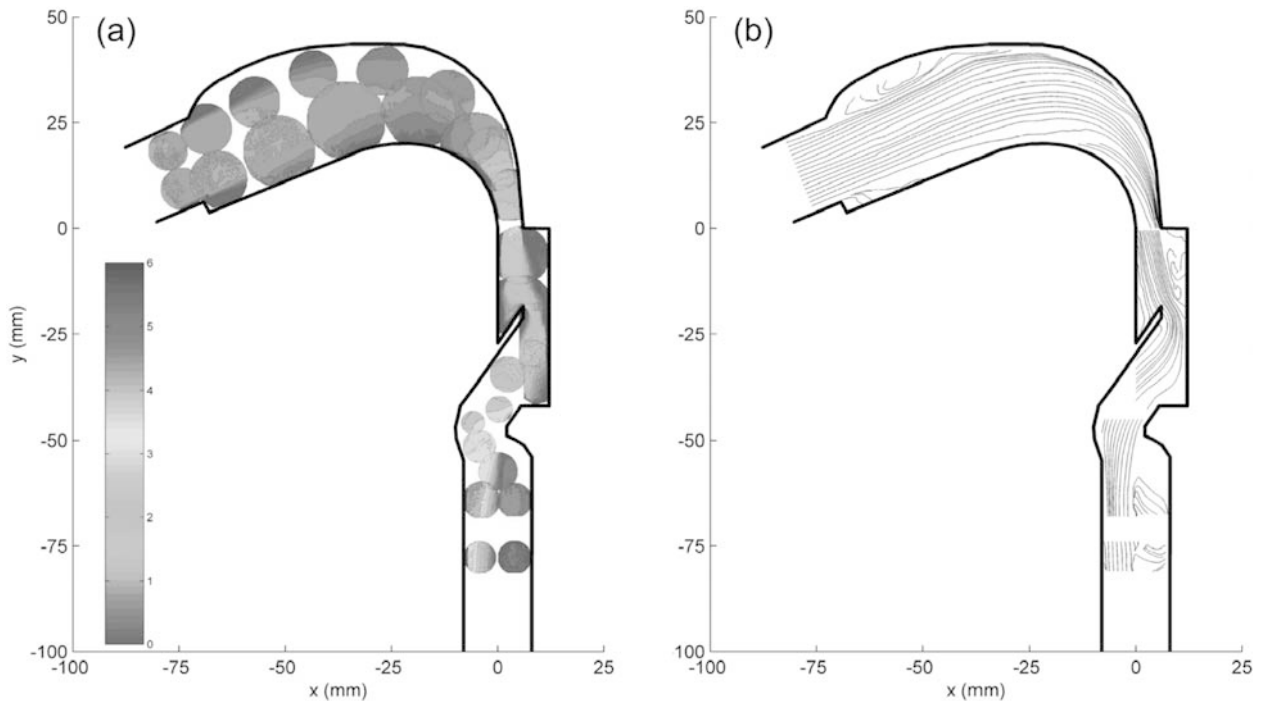
Fig. 10. Time-averaged measurements from PIV with an inhalation flow rate of 90 L/min: **a** time-averaged velocity magnitude normalized by the inlet plug-flow velocity; **b** 2-D streaklines

15 L/min) that the flow develops appreciably in that short distance.

The effect of decreasing Reynolds number can also be seen in Fig. 11, where the pressure drop across a full-scale model is plotted against the flow rate, Q. A line with a slope of 2, i.e., proportional to Q^2, is included for reference. At high Reynolds numbers, the pressure drop should be proportional to the square of flow rate, and the measurements above approximately 40 L/min follow the Q^2 line very closely. Below 40 L/min, the measured pressure
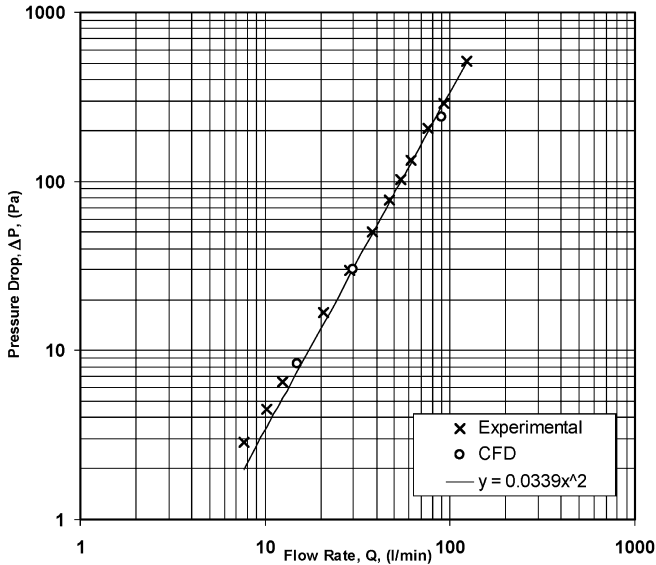
Fig. 11. Pressure drop against flow rate across a full-scale model

should be noted that this estimation is very sensitive to both positional and velocity measurement errors, particularly close to the wall, where PIV measurements are affected by wall glare. This calculation returns values of 1.34, 0.99, and 0.90 times the nominal flow rates for the 15, 30, and 90 L/min experiments respectively. The significant over-estimate for 15 L/min is surprising and may indicate that the 15 L/min inlet flow is appreciably non-axisymmetric.

5.3
Comparison with CFD

The experimental results indicated that significant flow development can occur upstream of the oral cavity at lower Reynolds numbers and, as a result, the velocity field boundary condition at the inlet to the oral cavity is not pure plug flow. To allow for this, CFD models were run with three different inlet boundary conditions. The first inlet boundary condition is plug flow at the inlet to the oral cavity without extension pipe and nozzle. The second is plug flow at the upstream end of the upstream pipe and nozzle arrangement. The third is the experimentally measured inlet velocity profile from the PIV results at the inlet of the oral cavity without the extension pipe and nozzle. Figures 12, 13, and 14 are time-averaged velocity magnitude and 2-D streamline plots for 30 L/min for these three inlet boundary conditions respectively.

The streamline plots indicate that the basic structure of the flow field is modeled quite well and that changing the inlet boundary condition has little effect on the modeled flow structure. All the major separation regions are well captured, although the CFD recirculation regions are
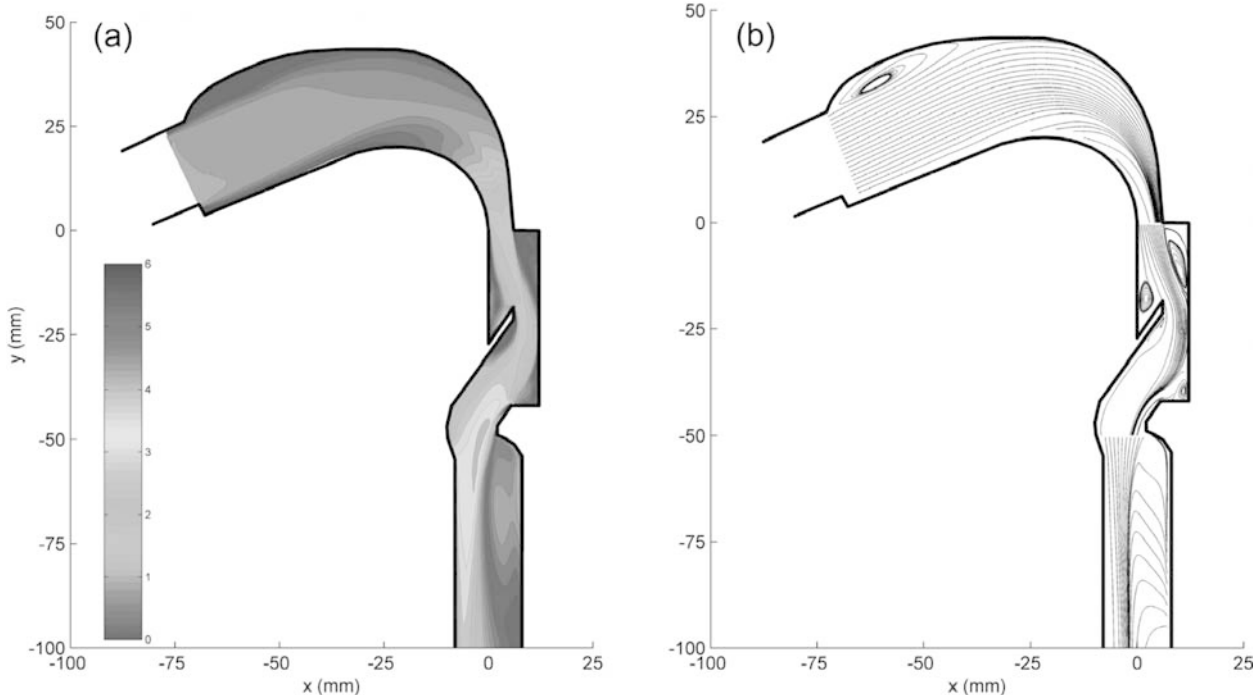
drop is greater than the Q^2 value, with the difference increasing with decreasing Q. It reaches about 30% higher at 15 L/min and nearly 100% higher at 8 L/min. This trend indicates increased retardation of the flow at lower Reynolds numbers, which is consistent with the PIV results.

The accuracy of the PIV measurements can be checked by extrapolating the (planar) PIV inlet velocity profiles around the circumference of the inlet and calculating a flow rate. This should return the nominal flow rate values, assuming, of course, the inlet flow is axisymmetric. It

Fig. 12a, b. CFD results for an inhalation flow rate of 30 L/min with a plug flow inlet boundary condition: **a** average velocity magnitude normalized by the inlet plug flow velocity, **b** 2-D streamlines
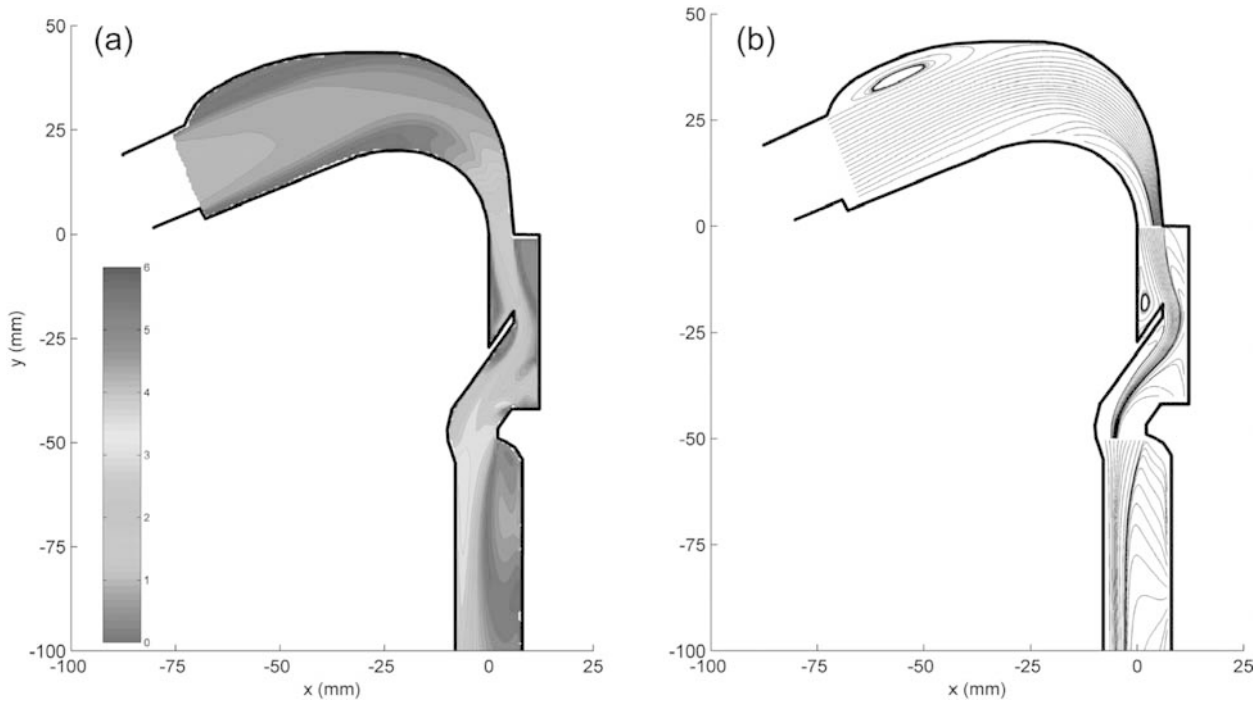
Fig. 13a, b. CFD results for an inhalation flow rate of 30 emin^{-1} with the geometry upstream of the inlet modeled: **a** average velocity magnitude normalized by the inlet plug flow velocity, **b** 2-D streaklines
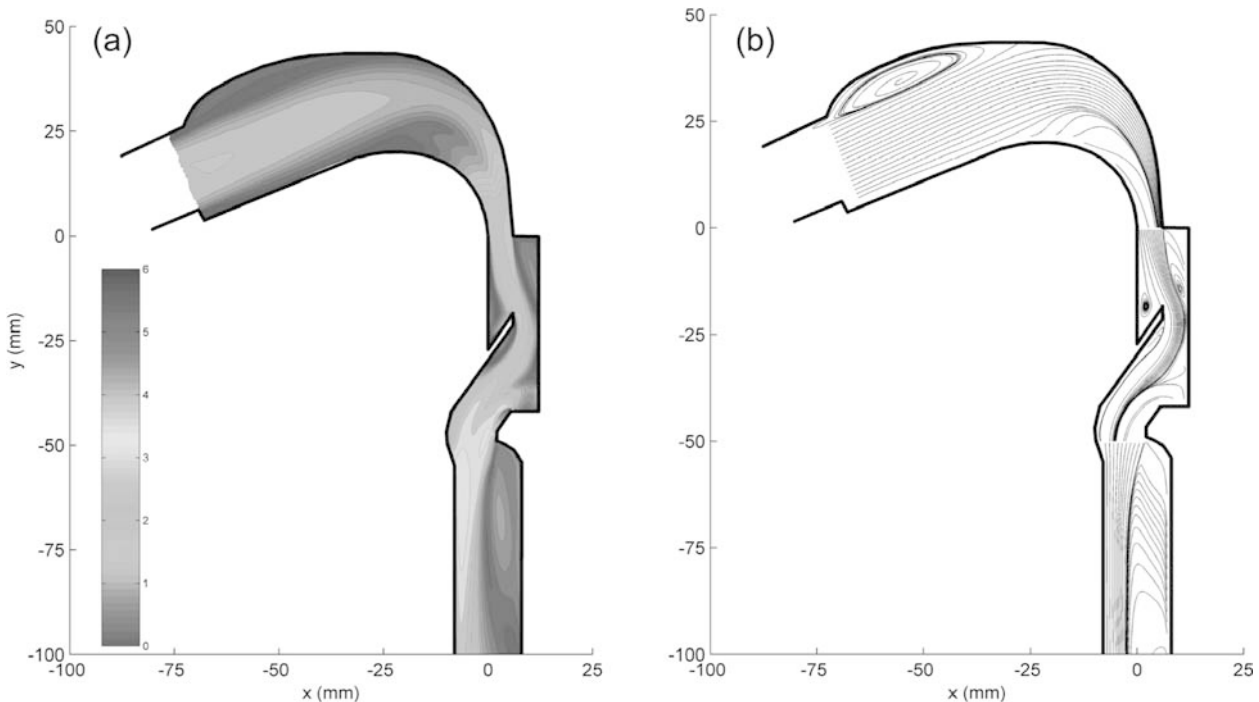

Fig. 14a, b. CFD results for an inhalation flow rate of 30 L/min with the experimentally measured inlet velocity profile: **a** average velocity magnitude normalized by the inlet plug flow velocity, **b** 2-D streaklines

generally slightly larger than the experimental ones. The non-conventional structure of the separated flow in the trachea is indicated in the CFD streakline patterns, and 3-D vector plots of the CFD field show the counter-rotating flow behavior here and also the Dean flow motion in the lower oral cavity. The CFD streaklines also show a small separation bubble at the junction of the epiglottis and anterior pharynx wall. This feature is not present in the
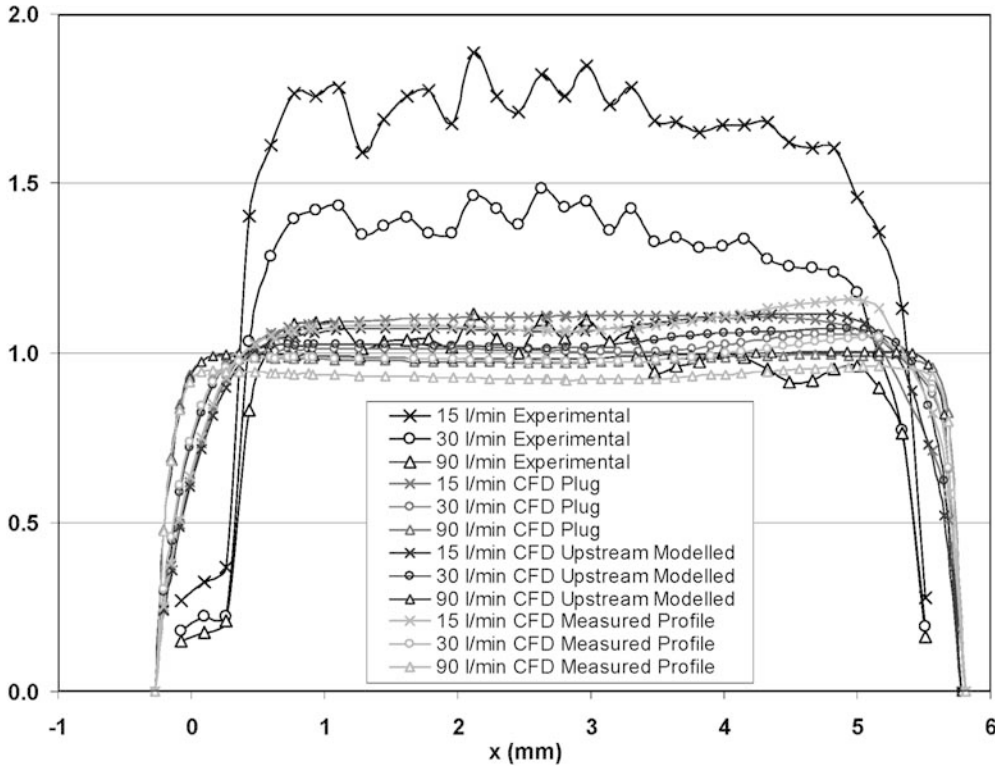
Fig. 15. Comparison of velocity magnitude profiles in oral cavity contraction at $y=2.5$ mm. The profiles are normalized by the local plug flow velocity

experimental mean streaklines, although this may be due to the fact that PIV measurements were particularly noisy in this region, owing to glare from the nearby solid surfaces. A recirculation region was occasionally visible in the instantaneous PIV results.

The effects of the different inlet conditions on velocity magnitude are largely confined to the oral cavity. The velocity magnitude plots for all three inlet conditions are reasonably similar to one another in the pharynx and trachea. However, core velocities in the CFD magnitude plots are much lower than the experimental results for 30 L/min, and actually more closely resemble the experimental results for 90 L/min. Indeed, for all three inlet conditions, the velocity magnitude field did not appreciably change with decreasing Reynolds number from the high-Reynolds-number state. This is in marked contrast to the experimental results.

This discrepancy is best illustrated in the downstream end of the oral cavity where the narrow cross-section accentuates the changing viscous effects due to varying Reynolds number. Figure 15 compares velocity profiles across the contraction at $y=2.5$ mm for all PIV and CFD results. They have been normalized against the local plug flow velocity, which is the flow rate divided by the local cross-sectional area, and have values of 2.24, 4.48, and 13.44 m/s for the 15, 30, and 90 L/min tests respectively. At the highest Reynolds number, the experimental profile approaches the plug flow condition, but as the Reynolds number decreases, core velocities increase significantly. Unfortunately, it is not possible to see clearly the changes in the boundary layers themselves, as the experimental results very close to the wall are erroneous due to wall glare. The CFD results also show an increase in core velocity, but it is very small—about an order of magnitude

smaller than seen in the experimental results. The major changes in inlet boundary condition have little effect, suggesting that this discrepancy is intrinsic to the modeling method and not the result of inaccurately defined boundary conditions.

The flow regime, particularly at the lower flow rates, may be transitional, and solutions for three inlet boundary conditions were also obtained using a laminar flow assumption. However, the discrepancies between these solutions and the experimental results were greater than for the solutions involving turbulence models.

6
Discussion

The magnitude of the Reynolds number effect in the PIV results was quite surprising and, as the PIV results are being used for validation, the experimental systems and methods were carefully scrutinized to ensure that the effect was not some kind of experimental error. It seems unlikely that the effect is the result of a PIV measurement or analysis problem. The measurements were carried out immediately after one another, using an identical procedure, with only Δt changing between measurements. The other possibility is that the flow rates through the model were not the nominal values. However, the flow rate was measured by two independent devices, and errors due to leaks etc. would tend to negatively bias the velocity magnitudes rather than increase them, and this kind of error would be expected to be greater at higher flow rates. Therefore, it is concluded that the discrepancy between the experimental and CFD results is due to errors with the CFD modeling.

The reasons for the errors in the CFD modeling are not clear. A likely cause appears to be inadequate boundary

layer modeling. The boundary layers in the present geometry are non-equilibrium and often in the very early stages of development, due to the many regions of separation and reattachment. If the growth of these new boundary layers is not accurately captured, it could lead to the discrepancies found between the PIV and CFD results. Furthermore, the flow field at lower Reynolds numbers may be transitional, which is very difficult to model with available RANS turbulence models. Also, the flow field is highly curved in many regions. This can result in significant anisotropic turbulence, which is not adequately captured by most of the turbulence models tested in this work.

One option would be to reduce the complexity of the idealized geometry and resulting flow field to see if better RANS modeling can be achieved. However, PIV experiments in realistic HOP geometries (submitted, Heenan et al. 2003) indicate that the complex flow features in this geometry are also present in anatomically correct HOP geometries and, indeed, the flow fields in realistic geometries HOP may be even more complex. Reducing the complexity of an idealized model may seriously compromise its validity as an accurate representation of HOP flow.

These problems with CFD modeling, which were obtained using best-practice methods, have significant ramifications for any subsequent particle deposition modeling. The velocity field in the near-wall region, where local deposition is primarily determined, is not being captured well (at least at lower Reynolds numbers). These problems must be addressed before RANS CFD/particle tracking becomes a robust tool for predicting particle deposition in actual in vivo conditions.

7
Conclusion

The mean and the turbulence RMS velocities in the central sagittal plane of an idealized representation of the human oropharynx were measured experimentally using endoscopic PIV for three different inhalation flow rates: 15, 30, and 90 L/min. Using CFD, the same flow-field was solved using RANS turbulence models. The results illustrate the complex nature of HOP flow, with three-dimensionality and several regions of separation and recirculation present. Comparison of the experimental and computational results shows that, although the RANS CFD reproduces the basic structure of the flow quite accurately, it does not capture well the increased viscous effects at lower Reynolds numbers. The results demonstrate the need for more development and validation of CFD modeling, particularly RANS models, in these flows.

References

Berger SA, Talbot L, Yao L-S (1983) Flow in curved pipes. Annu Rev Fluid Mech 15:461–512

Brancatisano T, Collett P, Engel L (1983) Respiratory movements of the vocal cords. J Appl Physiol 43:603–611

Corcoran TE, Chigier N (2000) Characterization of the laryngeal jet using phase Doppler interferometry. J Aerosol Med 13:125–137

DeHaan WH, Finlay WH (2001) In vitro monodisperse deposition in a mouth and throat with six different inhalation devices. J Aerosol Med 14:361–367

Dierksheide U, Meyer P, Hovestadt T, Hentschel W (2001) Endoscopic 2-D flow field measurements in IC engines. Paper 1060, presented at the Fourth International Symposium on Particle Image Velocimetry (PIV), Göttingen, Germany

Grotjans H, Menter FR (1998) Wall functions for general application CFD codes.In: Papailiou KD et al (eds) ECCOMAS 98 Proceedings of the 4th European CFD Conference. John Wiley, Chichester, pp 1112–1117

Hahn I, Scherer PW, Mozell MM (1993) Velocity profiles measured for airflow through a large scale model of the human nasal cavity. J Appl Physiol 75:2273–2287

Heyerichs K, Pollard A (1996) Heat transfer in separated and impinging turbulent flows. Int J Heat Mass Transfer 39:2385

Hopkins LM, Kelly JT, Wexler AS, Prasad AK (2000) Particle image velocimetry measurements in complex geometries. Exp Fluids 29:91–95

Kato M, Launder BE (1993) The modeling of turbulent flow around stationary and vibrating square cylinders. Proceedings of the 9th Symposium on Turbulent Shear Flows, Kyoto, pp 10-4-1–10-4-6

Katz IM, Martonen TB (1996) Flow patterns in three-dimensional laryngeal models. J Aerosol Med 9:501–511

Keane RD, Adrian RJ (1992) Theory of cross-correlation analysis of PIV images. Appl Sci Res 49:191–215

Li W-I, Perzl M, Heyder J, Langer R, Brain JD, Englmeier K-H, Niver RW, Edwards DA (1996) Aerodynamics and aerosol particle deaggregation phenomena in model oral-pharyngeal cavities. J Aerosol Sci 27:1269–1286

Melling A (1997) Tracer particles and seeding for particle image velocimetry. Meas Sci Technol 8:1406–1416

Menter FR (1994) Two-equation eddy-viscosity turbulence models for engineering applications. AIAA J 32:1598–1605

Nauwerck A, Gindele J, Spicher U, Rosskamp H, Landwehr (2000) Investigation of the transient in-cylinder flow inside a two stroke engine with particle image velocimetry. SAE Technical Paper 2000-01-0902, presented at the SAE 2000 World Congress, Detroit, Mich.

Nogueira J, Lecuona A, Rodriguez PA (1997) Data validation, false vectors correction and derived magnitudes calculation on PIV data. Meas Sci Technol 8:1493–1501

Olson DE, Sudlow MF, Horsfield K, Filley GF (1973) Convective patterns of flow during inspiration. Arch Intern Med 131:51–57

Raffel M, Willert C, Kompenhans J (1998) Particle image velocimetry—a practical guide. Springer, New York Berlin Heidelberg, ISBN 3-540-63683-8

Renotte C, Bouffioux V, Wilquem F (2000) Numerical 3D analysis of oscillatory flow in the time-varying laryngeal channel. J Biomech 33:1637–1644

Sarangapani R, Wexler AS (2000) Modelling particle deposition in the extrathoracic airways. Aerosol Sci Technol 32:72–89

Scarano F, Riethmuller ML (1999) Iterative mulitgrid approach in image processing with discrete window offset. Exp Fluids 26: 513–523

Speziale CG, Gatski TB (1993) Explicit algebraic stress models for complex turbulent flows. J Fluid Mech 254:59–78

Stahlhofen W, Rudolf G, James AC (1989) Intercomparison of experimental regional aerosol deposition data. J Aerosol Med 2:285–308

Stapleton KW, Guentsch E, Hoskinson MK, Finlay WH (2000) On the suitability of k–ε turbulence modeling for aerosol deposition in the mouth and throat: a comparison with experiment. J Aerosol Sci 31:739–749

Wernet M (2000) A flow field investigation in the diffuser of a high-speed centrifugal compressor using particle image velocimetry. Meas Sci Technol 11:1007–1022

Wilcox DC (1988) Reassessment of the scale determining equation for advanced turbulence models. AIAA J 26:1299–1310

Yu G, Zhang Z, Lessman R (1998) Fluid flow and particle diffusion in the human upper respiratory system. Aerosol Sci Technol 28: 146–158